J. Eur. Opt. Society-Rapid Publ. 2026, **22**, 53

https://doi.org/10.1051/jeos/2026046
Available online at: https://jeos.edpsciences.org

Journal of the European Optical Society-Rapid Publications

EOSAM 2025
Guest editors: Omar El Gawhary, Stefan Witte, Ignacio Moreno

RESEARCH ARTICLE OPEN ACCESS

Determining the health state of a single exosome via nano-coated silica microresonator

Maíra Martins Garcia, Brahim Bessif, Daniel Erni, and Mandana Jalali*

General and Theoretical Electrical Engineering (ATE), University of Duisburg-Essen (UDE) and Center for Nanointegration Duisburg-Essen (CENIDE), D-47048 Duisburg, Germany

Received 30 January 2026 / Accepted 10 May 2026

Abstract. We present a numerical study of a nanocoated whispering-gallery-mode (WGM) silica microdisk as a label-free platform for single-exosome detection and refractive-index–based health-state classification. The device is modeled as a fiber-coupled silica microdisk in water, functionalized with a thin nanocoating of either polystyrene (PS) or the metal-halide perovskite $CsPbI_3$. Using full-wave driven-mode simulations in Comsol Multiphysics, we show that nanocoatings reshape the WGM field distribution and improve sensing-relevant figures of merit by enhancing surface-field confinement while preserving high-Q_f operation. Beyond the field-pulling mechanism provided by polymer coatings, we demonstrate a distinct sensitivity enhancement enabled by perovskites: spectral alignment of the WGM with an excitonic resonance in $CsPbI_3$ supports a hybrid excitonic–photonic mode that concentrates optical energy at the sensing interface and increases the transduction of minute effective-refractive-index (ERI) variations into measurable resonance shifts. To connect the exosome composition to the optical response, we introduce a physics-based workflow to estimate dispersive ERIs of individual exosomes from their protein and nucleic-acid content using a Barer-type relation and a core–shell geometry, and we map these ERIs to resonance-wavelength shifts for single exosomes at the sensing position. The resulting resonance signatures provide separable responses for healthy-like, borderline, and cancer-like exosomes, indicating that the proposed excitonically engineered WGM microresonator can not only detect single exosomes but also classify their health state, supporting a route toward non-invasive liquid-biopsy diagnostics.

Keywords: Whispering gallery mode (WGM) microresonator, Nanocoating, Polystyrene, Perovskite, Exosome health state, Excitonic-photonic coupling.

1 Introduction

Optical biosensors that enable direct, real-time, non-invasive and label-free detection of bioelements are highly desired in biological studies. These sensors require ultra-sensitive mechanisms to detect single nanoscale particles and, when the goal is specificity, should also detect and distinguish even small variations in the particle's composition. In this regard, optical microresonators, sustaining whispering gallery modes (WGMs) have been established as ultra-sensitive sensors and are the appropriate candidates for such task.

The first demonstrations of using WGM microresonators for biosensing emerged in the early 2000s, such as the 2002 report by Vollmer et al. on protein detection using a resonant microcavity and the 2003 study by Arnold et al. discussing the frequency shifts induced by protein adsorption in microspheres sustaining WGMs [1, 2]. Since then, interest in using WGM-based biosensors has increased substantially, and major advances in both sensing mechanisms and experimental techniques have been made [3–6].

Therefore, WGM biosensing has developed into a central platform for label-free biological and chemical sensing, owing to their ultra-high quality factors (Q_f), small mode volumes (V_{mode}), and strong electric field intensity at the sensing location $|\boldsymbol{E}|$. A wide variety of ultra-high Q_f WGM microresonator designs have already been fabricated, with various geometries including microspheres, microdisks, microrings, microtoroids, microbubbles, microbottles, and microcapillaries, presenting ultra-high Q_f values in the range of 10^4–10^{10} [3–5, 7, 8].

Comprehensive reviews report applications of WGM microresonators ranging from bulk refractometry and protein binding to single virus and nanoparticle detection, as well as recent progress towards integrated and optofluidic implementations for clinical diagnostics [3, 6, 7, 9–11]. More specifically, for single-molecule and single-particle detection, WGM biosensors have also been applied to sense

* Corresponding author: mandana.jalali@uni-due.de

nucleic acids (NAs), antibodies, and extracellular vesicles (EVs) such as exosomes [12–14]. For EVs and exosomes in particular, microtoroid WGM resonators have enabled real-time, label-free single-exosome detection in complex media [13], complementing other optical platforms such as interferometric imaging and nanoparticle-tracking-based methods [15–17]. Collectively, these characteristics established WGM-mode microresonators as an attractive platform for single-nanoparticle detection and characterization.

Exosomes are of particular interest for diagnostics because their molecular cargo reflects the physiological and pathological state of their parent cells, making them promising biomarkers for a range of diseases, including cancer [18, 19]. This property supports early-stage disease detection through non-invasive or minimally invasive liquid biopsies, as exosomes can be isolated from readily accessible body fluids such as blood, saliva, and urine [20, 21]. Tumor-derived exosomes often carry altered protein and nucleic-acid signatures compared with exosomes from healthy cells, which can manifest as subtle shifts in their effective refractive index (ERI); such shifts are, in principle, detectable with WGM-based biosensors and may enable cancer diagnosis [22–24]. Nevertheless, direct phenotyping and robust health-state classification remain challenging due to the small size of exosomes (typically 30–150 nm) and their low refractive-index contrast relative to the surrounding medium [25–27].

Recent optical studies have begun to quantify the ERI of extracellular vesicles (EVs) and to correlate subtle ERI variations with differences in biochemical composition [17, 25, 26]. In parallel, a range of hybrid and coated WGM architectures, including plasmonic-enhanced resonators, high-index coatings, and polymer microlaser platforms, have been proposed to further localize the optical field at the sensor surface and to push detection limits toward the single-molecule regime [28–30]. Metal-halide perovskites have emerged as particularly attractive high-index, excitonic materials, enabling high-Q_f WGM lasing and strong exciton–photon coupling in $CsPbX_3$ and $FAPbX_3$ microcavities [31–35]. However, to the best of our knowledge, perovskite nanocoatings have not yet been leveraged to engineer WGM microresonators specifically for exosome sensing, nor has ERI-based classification of individual exosomes been explored using such hybrid structures.

The goal of this work is to discriminate the health state (cancerous versus healthy) of single exosomes using coated WGM microresonators. Realizing this capability would enable an early-stage, non-invasive, label-free biosensing approach to cancer diagnostics based on liquid biopsy. Achieving robust single-exosome classification requires further improvements in the sensing limit of optical microresonators. A particularly effective strategy is to introduce a carefully engineered nanocoating with a refractive index higher than that of the underlying resonator. We have previously shown that such high-index nanocoatings can enhance sensing performance by pulling the supported modes toward the coating region, increasing Q_f and $|\boldsymbol{E}|$, and simultaneously reducing the effective mode volume V_{mode} [36–38]. Results show that, depending on the coating material, $|\boldsymbol{E}|$ can be amplified by up to a factor of 2.25 relative to the uncoated microresonator, V_{mode} can be reduced by 21%–77%, and Q_f can increase from approximately 5×10^4 (uncoated) up to 8×10^7 for the case of Si_3N_4 nanocoating [36].

In this work, microdisks with tailored nanocoatings are modeled and simulated using the finite-element method (FEM)-based simulation platform Comsol Multiphysics. Full-wave, driven-mode simulations are performed, in which WGMs are excited in the microresonator via fiber optic coupling. Although computationally demanding, this modeling approach allows a comprehensive investigation of the impact of the nanocoating on the microresonator characteristics and enables precise calculation of the resonance wavelength shifts induced by the presence of healthy and cancerous exosomes. A 30 μm silica microdisk in an aqueous medium is considered, to which a 100 nm-thick nanocoating of either a polymer or a perovskite material is added. The sensing performance of the uncoated microresonator, the polymer-coated microresonator and the perovskite-coated microresonator is evaluated in terms of Q_f, mode volume, coupling efficiency and electric field strength at the sensing location.

Additionally, we introduce and implement a novel approach for determining the effective refractive index (ERI) of exosomes via numerical simulations. This method yields a dispersive ERI for healthy and cancerous exosomes, as well as for exosomes whose ERI lies in the borderline region between the two health states. These exosomes are then placed in the near field of the modeled microresonators and the resulting resonance wavelength shifts are computed.

Our results show that selecting a suitable perovskite material with a bandgap around the WGM resonance wavelengths of the microresonator enables strong photonic–excitonic interaction between the perovskite coating and the resonator, leading to a substantial enhancement of the quality factor. These improvements, in turn, enable the detection of very small variations in the exosomes' ERI and thereby the determination of the health state of individual exosomes.

The rest of the paper is organized as follows. In Section 2, the nanocoating concept is discussed in detail and the choice of nanocoating materials is explained. Section 3 introduces exosomes and our approach to determine their ERI in different health states; the modeling details and the resulting dispersive ERIs are presented there. The microresonator modeling and simulations are described in Section 4, while the impact of the nanocoating on the microresonator performance is analyzed in Section 5. In Section 6, single exosomes are positioned next to the microresonators and the corresponding resonance wavelength shifts are evaluated. Finally, Section 7 summarizes the main conclusions and provides an outlook on future work.

2 The nanocoating

The rationale for introducing a high-refractive-index nanocoating is to directly engineer the three figures of merit that determine the resonance shift of whispering-gallery–

mode (WGM) microresonators, namely the quality factor Q_f, the mode volume V_{mode}, and the local electric field intensity at the sensing location $|E(\boldsymbol{r})|^2$. Rather than modifying the resonator geometry, we add a thin nanocoating with refractive index $n_{coat} > n_{SiO_2}$ around the silica microresonator. An extensive material study among dielectrics, polymers, quantum dots, and perovskites, based on their dispersive refractive indices and, in the cases of quantum dots and perovskites, their bandgaps, showed that appropriate candidates for our purpose are silicon nitride Si_3N_4 and titanium dioxide TiO_2 (dielectrics), polystyrene (PS; polymer), cadmium selenide (CdSe) and cadmium zinc (CdZn) quantum dots, as well as cesium lead triiodide ($CsPbI_3$) perovskite. The corresponding dispersive refractive indices and extinction coefficients of these materials, together with the refractive index of silica as the baseline, obtained from Ref. [39, 40], are illustrated in Figure 1. Among the investigated materials, the PS polymer and the $CsPbI_3$ perovskite are chosen as the nanocoating materials in this work.

2.1 Polymer coating (polystyrene)

In our earlier eigenmode analysis of coated silica microspheres, we systematically explored several high-refractive-index dielectric and polymer materials as candidate nanocoatings, namely TiO_2, Si_3N_4, and PS, with various thicknesses [36]. For each coating, the quality factor Q_f, the mode volume V_{mode}, and the normalized electric field at the sensing interface $|E_{norm}| = |E|_{surf}/|E|_{surf}^{(uncoated)}$ were obtained from our eigenmode models. All three nanocoatings led to an increase in Q_f and a reduction in V_{mode} compared to the uncoated microsphere, confirming the general effectiveness of the nanocoating concept for improving the sensitivity. However, the different materials exhibited distinct trade-offs between radiation-loss suppression and evanescent-field penetration into the surrounding sensing medium, i.e., the water in which the exosomes are suspended.

The highest-index TiO_2 nanocoating provided a strong suppression of radiative leakage and thus a substantial Q_f enhancement, together with a reduced mode volume, but the WGM was largely confined inside the nanocoating, which resulted in a diminished electric field at the outer interface. The Si_3N_4 nanocoating offered the best purely optical figures of merit within the eigenmode framework: it yielded the largest increase in Q_f, the smallest V_{mode} and an enhancement of the surface field by approximately a factor of two relative to the uncoated case. PS, on the other hand, produced a somewhat smaller Q_f enhancement, yet still reduced the mode volume and increased the surface field by a factor of ~2.25, while its refractive index, being closer to that of water ($n_{water} = 1.3264 + i4.29 \times 10^{-6}$ in the corresponding wavelength range), allowed the evanescent tail of the mode to penetrate more efficiently into the external sensing region [36]. This behaviour was also reflected in the radial field profiles, where the PS nanocoating shifted the mode towards the surface without overly confining it within the coating.

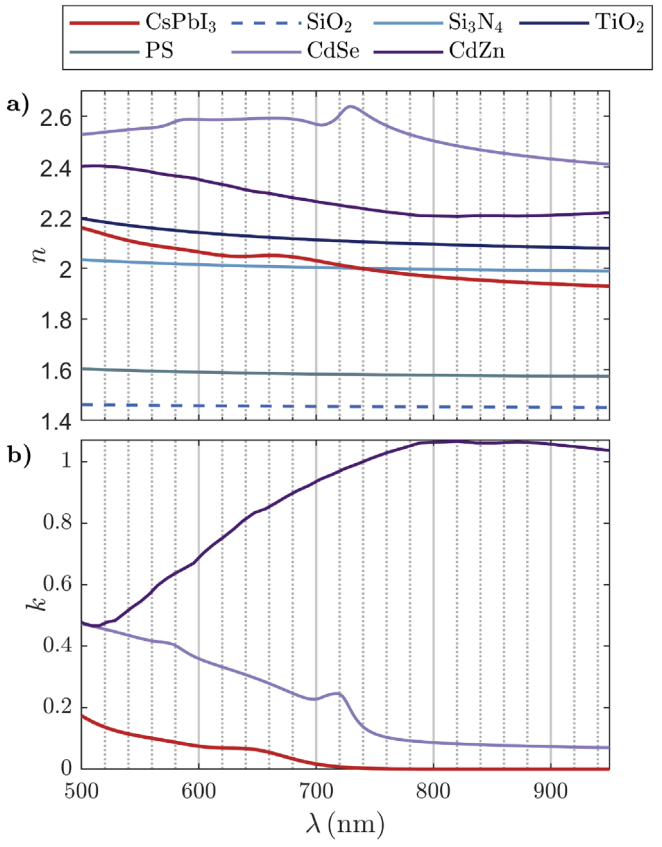

Figure 1. a) Dispersive refractive indices of SiO_2, Si_3N_4, TiO_2, PS, CdSe, CdZn, and $CsPbI_3$ versus wavelength, and b) the extinction coefficients for CdSe, CdZn, and $CsPbI_3$.

Beyond these optical metrics, practical fabrication considerations strongly favour polymer coatings for implementing nanocoatings on curved microresonators. High-index dielectric layers such as TiO_2 or Si_3N_4 typically require vacuum-based deposition techniques (e.g. CVD, ALD, sputtering) that can introduce surface roughness and residual stress, which in realistic devices reintroduce scattering losses and may compromise the high Q_f values predicted by ideal eigenmode simulations. In contrast, PS can be deposited by standard spin-coating or dip-coating from solution on silica substrates, yielding conformal nanocoatings with low surface roughness and good thickness control, and thus preserving the high intrinsic Q_f of the underlying resonator. Taking into account both optical performance and fabrication feasibility, we therefore selected PS as the polymer nanocoating material in the present work and use it as the reference system for comparison with higher-index perovskite coatings.

It is important to note that the initial material screening in Ref. [36] was performed in an eigenmode setting, which is ideal for extracting intrinsic Q_f and V_{mode} but does not explicitly include the excitation and out-coupling configuration. In an eigenmode formulation, the resonator is treated as a source-free open cavity, yielding complex eigenfrequencies $\tilde{\omega}$ and hence an intrinsic quality factor

$$Q_{\mathrm{int}} = \frac{\Re\left\{\tilde{\omega}\right\}}{2\,\Im\left\{\tilde{\omega}\right\}}, \tag{1}$$

together with the corresponding modal field profiles and V_{mode} for the isolated structure. This framework does not capture coupling-induced loading, mode selectivity under a specific excitation, nor the transmitted-spectrum line shape. By contrast, our full-wave driven-mode simulations explicitly launch the single-mode optical fiber (SMF) fundamental mode and compute the transmission T of the coupled fiber–microdisk system. The extracted linewidth therefore corresponds to the loaded quality factor Q_{L},

$$\frac{1}{Q_{\mathrm{L}}} = \frac{1}{Q_{\mathrm{int}}} + \frac{1}{Q_{\mathrm{ext}}}, \tag{2}$$

where Q_{ext} accounts for external coupling. This driven formulation enables optimizing the coupling gap d_x (under-/critical-/over-coupling) based on T, and it provides power-normalized field amplitudes at the sensing region under realistic excitation conditions, which is essential for quantitatively predicting exosome-induced resonance shifts. Accordingly, in the present study, these eigenmode-based design guidelines are validated and extended using full driven-mode simulations with explicit fiber-optic coupling. The driven-mode results confirm the qualitative trends found previously and demonstrate that PS nanocoatings indeed yield the expected enhancement of the exosome-induced resonance wavelength shifts under realistic excitation conditions.

2.2 Perovskite nanocoating and exciton–photon coupling

To further enhance the sensing performance in our approach beyond what is achievable with purely dielectric or polymer nanocoatings, we investigated whether an excitonic–photonic coupling between the microresonator whispering-gallery mode (WGM) and an excitonic transition in the nanocoating can be exploited. The basic idea is to choose a coating material that supports a pronounced excitonic resonance in the same spectral range as the fundamental WGM of the silica microresonator, such that the photonic mode hybridizes with the excitonic mode and forms mixed exciton–photon states with enhanced field confinement and a dispersive response at the sensor surface.

As a first step, we carried out a material screening of potential candidates for excitonic material systems, focusing on commercially available quantum-dot materials (CdSe, CdZn-based quantum dots) and metal-halide perovskites. Using reported dispersion data and bandgap energies (cf. Fig. 1b), we identified materials whose bandgaps lie in the vicinity of ~700 nm, i.e. close to the WGM resonance of our 30 µm silica microresonator in water. This analysis confirmed that CdSe and CdZn quantum dots as well as the perovskite $CsPbI_3$ exhibit excitonic transitions in the targeted spectral range. In a subsequent eigenmode study, each of these materials was introduced as a nanocoating with thicknesses in the range of 100–200 nm around the silica microresonator, and the resulting resonator figures of merit – the quality factor Q_{f}, the mode volume V_{mode} and the surface electric field $|\boldsymbol{E}|$ – were systematically evaluated.

The quantum-dot coatings, due to their relatively high extinction coefficients (cf. Fig. 1b), not only failed to achieve any clear photonic–excitonic coupling but also substantially degraded the photonic mode of the microresonator and, in several cases, prevented the formation of well-defined resonances. In contrast, the $CsPbI_3$ perovskite nanocoating led to a distinct photonic–excitonic coupling and accordingly provided the most pronounced simultaneous improvement of all sensing figures of merit. In the eigenmode simulations, the perovskite-coated resonator exhibited a substantial enhancement of Q_{f}, a compression of V_{mode} and a strong increase of the evanescent field at the outer interface compared to the uncoated resonator and the resonators with the best-performing polymer (PS) and dielectric (TiO_2, Si_3N_4) coatings [41]. The spectral dependence of the eigenfrequencies and field distributions indicated that the WGM of the silica core hybridizes with the excitonic resonance of the $CsPbI_3$ layer: close to the perovskite band edge, the mode is pulled into the coating, the effective index exhibits a pronounced dispersive feature and the field intensity at the coating–water interface is strongly amplified. These observations are consistent with an excitonic–photonic coupling mechanism rather than a purely geometric or index-contrast effect.

A natural concern when employing excitonic materials as microresonator coatings is their intrinsic loss: the strong oscillator strength that gives rise to the excitonic resonance is accompanied by a non-negligible imaginary part of the refractive index, which could in principle degrade the microresonator's Q_{f} and offset any sensitivity gain. For this reason, we explicitly compared all sensing criteria of the $CsPbI_3$-coated resonator against those of the PS and dielectric (TiO_2, Si_3N_4) nanocoatings. Despite its higher material loss, the $CsPbI_3$ coating was found to outperform all other options: in the spectral region where the WGM and excitonic resonance overlap, the perovskite nanocoating yields the highest Q_{f}, the smallest V_{mode} and the strongest surface field enhancement, which together translate into the largest resonance wavelength shift induced by a single exosome. These eigenmode-based findings, first reported in our earlier perovskite-coating study [41], are in the present work corroborated and extended by full driven-mode simulations with explicit fiber coupling. The results obtained within this fully numerical framework should be interpreted as a predictive assessment of the sensing performance under realistic excitation conditions, indicating that the excitonic $CsPbI_3$ nanocoating could significantly enhance the sensing functionality of silica microresonators.

The analysis presented here focuses on the idealized optical response of an intact $CsPbI_3$ nanocoating within a numerical design framework. Long-term chemical stability of bare $CsPbI_3$ in aqueous or electrolyte-containing biological environments is not assumed and remains a separate materials-engineering challenge. Practical implementation in biofluids will therefore require appropriate stabilization and encapsulation strategies for the perovskite shell, along with careful control of the local chemical environment.

3 Exosomes

Exosomes are nanoscale extracellular vesicles (EVs), typically ∼30–150 nm in diameter, released by most cell types through the endosomal pathway. They carry a rich molecular cargo of proteins, lipids, metabolites, and nucleic acids (DNA, mRNA, miRNA), which closely reflects the physiological and pathological state of their parental cells [18, 19]. Because exosomes are abundant and stable in virtually all biofluids (blood, urine, saliva, cerebrospinal fluid), they can be collected in a minimally invasive manner by liquid biopsy and are therefore highly attractive as early-stage cancer biomarkers [20, 21]. Tumour-derived exosomes exhibit characteristic alterations in their cargo composition – in particular in protein and nucleic-acid content – and encode cancer-type-specific signatures that can be exploited for diagnosis, patient stratification, and therapy monitoring [17, 23, 24].

From an optical-sensing perspective, these biochemical alterations manifest as subtle changes in the exosome's effective refractive index (ERI), which can in principle be detected by sufficiently sensitive label-free photonic biosensors [16, 42]. The present work builds on this concept by linking the protein and nucleic-acid (NA) content of single exosomes to their ERI and, in a second step, to the resonance response of high-Q_f WGM microresonators.

3.1 Core–shell geometric model of the exosome

A single exosome is modeled as a concentric core–shell sphere embedded in an aqueous host medium and numerically analyzed in Comsol Multiphysics. The core represents the lumen, an aqueous solution of proteins and nucleic acids (NA), while the shell represents the lipid bilayer membrane. Consistent with electron microscopy and membrane biophysics, the outer radius of the exosome is taken as $a = 45.5$ nm, and the lipid bilayer shell thickness as $t_{\text{shell}} = 5$ nm, so that the lumen radius is $b = a - t_{\text{shell}} = 40.5$ nm [43]. The lipid shell is modeled as a non-absorbing layer with slightly dispersive refractive index around $n_{\text{shell}} \simeq 1.48$ in the visible/near-IR, in line with spectroscopic studies of supported lipid bilayers and vesicles [44–47]. The host medium is taken as water with dispersive refractive index $n_{\text{water}}(\lambda)$ [48].

Within this framework, the only degrees of freedom that encode the biological state of the exosome are the lumen composition (protein and NA concentrations) and, to a lesser extent, the detailed lipid composition of the membrane. In this study we focus on the lumen composition as the primary contrast mechanism between healthy-like and cancer-derived exosomes.

3.2 Lumen refractive index from the Barer relation

The refractive index of the exosome lumen is computed in MATLAB using the classical two-substance (Barer) relation for aqueous macromolecular solutions [49]. For an aqueous mixture of proteins and nucleic acids at mass concentrations c_{prot} and c_{NA} (in g mL^{-1}), the lumen refractive index can be written as

$$n_{\text{core}}(\lambda) = n_{\text{water}}(\lambda) + \left(\frac{\mathrm{d}n}{\mathrm{d}c}\right)_{\text{prot}} c_{\text{prot}} + \left(\frac{\mathrm{d}n}{\mathrm{d}c}\right)_{\text{NA}} c_{\text{NA}}, \quad (3)$$

where $(\mathrm{d}n/\mathrm{d}c)_{\text{prot}}$ and $(\mathrm{d}n/\mathrm{d}c)_{\text{NA}}$ are the refractive-index increments (RII) of proteins and nucleic acids, respectively. In the visible range at ambient temperature, robust consensus values are $(\mathrm{d}n/\mathrm{d}c)_{\text{prot}} \approx 0.190$ mL g^{-1} and $(\mathrm{d}n/\mathrm{d}c)_{\text{NA}} \approx 0.170$ mL g^{-1}, with only weak dispersion [50, 51].

Guided by experimental reports that place the effective refractive index of extracellular vesicles in the range $n_{\text{eff}} \approx 1.37$–$1.40$ in the visible [16, 26, 42], we select biologically plausible concentration bands for healthy-like and cancer-like exosomes. Healthy-like exosomes are assigned protein and NA concentrations in the lower part of the band, while cancer-derived exosomes are assigned elevated concentrations, consistent with the increased protein and NA cargo typically observed in tumour-derived EVs [21, 52]. Evaluating equation (3) for these concentration bands yields three representative lumen refractive indices: $n_{\text{core}}^{(\text{H})}(\lambda)$ for healthy exosomes, $n_{\text{core}}^{(\text{C})}(\lambda)$ for cancerous exosomes, and intermediate values $n_{\text{core}}^{(\text{B})}(\lambda)$ for "borderline" exosomes whose protein/NA content lies between the two regimes.

Figure 2 summarizes the resulting $n_{\text{core}}(\lambda)$ for these three classes in the wavelength range relevant to our microresonator WGMs.

3.3 Effective refractive index of the whole exosome

To obtain an effective refractive index for the entire exosome (core plus lipid shell), a full-wave driven-mode simulation of the core–shell sphere in Comsol Multiphysics is carried out. The reason for considering exosomes as core–shell structures is to increase the sensitivity to the slightest changes in the core, i.e. variations in the protein/NA content. Consistent with this modeling objective, variations in the lipid bilayer are not explicitly included, and the membrane is treated as having fixed thickness and refractive index. While biologically relevant variations in membrane composition may also contribute to the overall effective refractive index of the exosome, this effect is beyond the scope of the present study and will be addressed in future sensitivity analyses. Within this framework, the model can be regarded as conservative, as it isolates the lumen contribution and enables a clear characterization of lumen-composition-induced contrast.

The core–shell exosome model described above is illuminated by a plane wave in the 500–900 nm spectral range, and the electric field $\boldsymbol{E}(\boldsymbol{r})$ and the electric flux density $\boldsymbol{D}(\boldsymbol{r})$ inside the whole exosome volume V_p (core plus shell) are computed. The effective relative permittivity of the exosome is then retrieved via

$$\varepsilon_{\text{eff}} = \frac{\langle \boldsymbol{D}(\boldsymbol{r}) \rangle}{\varepsilon_0 \langle \boldsymbol{E}(\boldsymbol{r}) \rangle}, \quad (4)$$

where ε_0 is the vacuum permittivity and $\langle \cdot \rangle$ denotes a volume average over V_p. The effective refractive index of the exosome is then obtained as

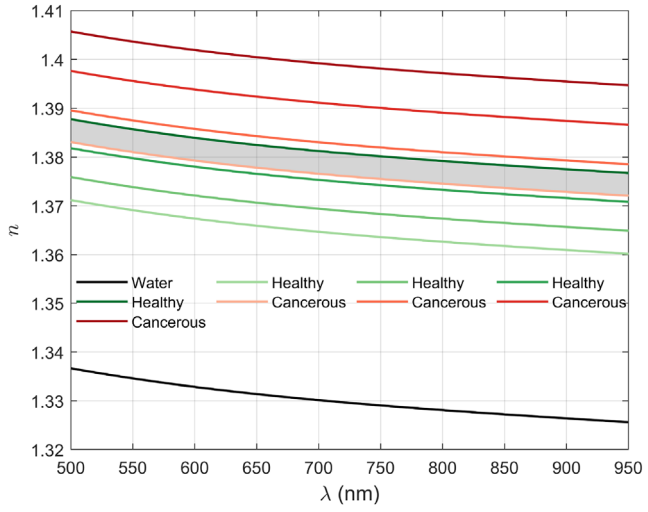

Fig. 2. Computed lumen refractive index n_{core} (λ) for healthy-like (H), borderline (B), and cancer-like (C) exosomes based on the Barer relation and protein/NA concentration bands.

$$n_{\text{eff}}(\lambda) = \sqrt{\varepsilon_{\text{eff}}(\lambda)}. \tag{5}$$

This procedure is applied to the healthy-like, borderline, and cancer-like lumen compositions defined above, thereby yielding three effective refractive indices $n_{\text{eff}}^{(\text{H})}(\lambda)$, $n_{\text{eff}}^{(\text{B})}(\lambda)$, and $n_{\text{eff}}^{(\text{C})}(\lambda)$.

The retrieved indices are consistent with the expected extracellular vesicle (EV) optical responses and fall within the experimentally observed EV index range (~1.37–1.40 in the visible) reported by nanoparticle tracking analysis and flow cytometry [16, 26, 42, 53].

Figure 3 shows the resulting effective refractive indices for the three exosome classes at the wavelengths of interest. Cancer-derived exosomes systematically exhibit a slightly higher n_{eff} than healthy-like exosomes, with borderline exosomes (gray shaded area in the Fig. 2) populating the intermediate range. These distinct ERI bands form the basis for the single-exosome classification strategy pursued in this work, where the exosomes, modeled as homogeneous spheres with the retrieved n_{eff}, are placed in the near field of uncoated, PS- and $CsPbI_3$-coated silica microresonators to calculate the corresponding resonant wavelength shifts.

4 Modeling and simulation

All models are built in Comsol Multiphysics, which relies on the Finite-Element Method (FEM). The proposed biosensor is a silica microresonator (microdisk, 30 μm radius) with a 100 nm coating, placed in an aqueous medium. Light is coupled into the microdisk via a single-mode optical fiber (SMF), consisting of a silica core of 500 nm radius and a Teflon cladding of 2 μm thickness, designed and optimized in our previous works [37, 38]. A two-dimensional modeling approach was used, and the input power applied in the SMF optical fiber was 1 W/m for all models. A schematic representation of the modeled microresonator is shown in Figure 4.

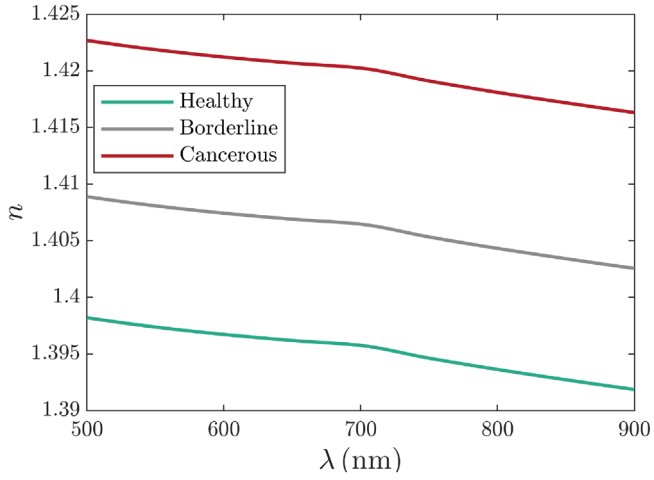

Fig. 3. Effective refractive indices n_{eff} of healthy-like (H), borderline (B), and cancer-like (C) exosomes retrieved from the full-wave Comsol Multiphysics simulations.

In order to ensure the accuracy of the results and explicitly account for the effect of light coupling into the microresonator, all simulations are performed in a full-wave driven-mode configuration. To the best of our knowledge, we are the first group to demonstrate such full-field driven-mode simulations of coated WGM microresonators [37, 38]. Three modeling scenarios are investigated: an uncoated microdisk, which provides the baseline for all comparisons; a PS-coated microdisk; and a $CsPbI_3$-coated microdisk. In each case, the coupling distance d_x, the distance from the fiber core to the microresonator, is optimized to maximize the coupling efficiency. Specifically, we choose a d_x that maximizes the transmitted power T while maintaining a high quality factor Q_{f}.

For every model, the relevant figures of merit are extracted, namely the resonance wavelengths λ_{res}, the transmitted power T, the quality factor Q_{f}, the mode volume V_{mode}, and the electric-field at the sensing location $|\boldsymbol{E}|$. These quantities are used to quantify and compare the sensing functionality of the biosensor in the uncoated, PS-coated, and $CsPbI_3$-coated cases. Afterwards, a single exosome is placed in the immediate vicinity of the microresonator equator for the three health states – healthy (H), borderline (B), and cancerous (C) – and the corresponding resonance wavelength shifts $\Delta\lambda_{\text{res}}$ are calculated. By immediate vicinity, we mean that, in each case, the exosome is positioned in direct, tangential contact with the microresonator boundary at the equator, on the right-hand side of the resonator in Figure 4. This enables a direct assessment of the sensing performance of uncoated and nanocoated microresonators for single-exosome classification.

It is worth mentioning that such multiscale full-wave driven-mode simulations (microresonator in the micrometer regime, coating and exosome in the nanometer regime) require an extremely well-designed and fine mesh, in particular in the fiber–microresonator coupling region, and around the coating and exosome. To ensure accuracy and consistency, the same meshing strategy is used for all models. This requirement results in 1,766,528 mesh elements

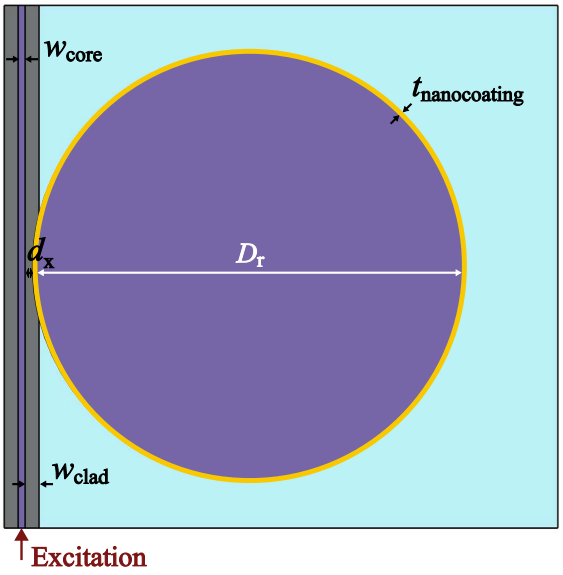

Fig. 4. Schematic of the biosensor: a 30 μm microdisk with a 100 nm coating in aqueous medium. Light is coupled into the microdisk via an optical fiber, where the coupling distance d_x is the key coupling parameter.

with an average mesh quality of 0.89. Each simulation run takes about 328 min (approximately 5 h 28 min) on a workstation equipped with an AMD Ryzen 9 7950X 16-core processor, and 96 GB of RAM.

5 Effects of the nanocoating

As a first step, the uncoated microresonator is modeled and simulated. It is found that the optimal coupling distance between the core of the optical fiber and the microresonator is $d_{x,u} = 350$ nm, for which 85.6% of the incoming power is coupled into the microresonator. The corresponding resonance wavelength is $\lambda_{res,u} = 786.92$ nm with a quality factor of $Q_f = 1.81 \times 10^4$ [38]. The electric-field intensity of this configuration at $\lambda_{res,u}$ is shown in Figure 5, together with a zoomed view of the z-component of the electric field that clearly illustrates the excited mode.

5.1 PS coating

Next, the PS-coated microresonator is modeled and simulated. In this case, the best coupling is obtained for the distance $d_{x,PS} = 400$ nm, for which 92.4% of the incoming power is coupled into the microresonator. The resonance wavelength is $\lambda_{res,PS} = 789.38$ nm, and the electric-field intensity at resonance is shown in Figure 6. It can be observed that the presence of the coating attracts the optical mode towards the coating layer and thereby amplifies the evanescent tail of the electric field in the water region.

The sensing figures of merit for this configuration are summarized in Table 1. The results show that the PS nanocoating enhances the biosensor performance compared to the uncoated case by increasing Q_f by about 15%, reducing the mode volume by 25.8%, and amplifying the electric-field intensity at the sensing location by a factor of 1.75, as already reported in [38]. These results demonstrate that the addition of the 100 nm PS coating significantly improves the sensing functionality of the microresonator.

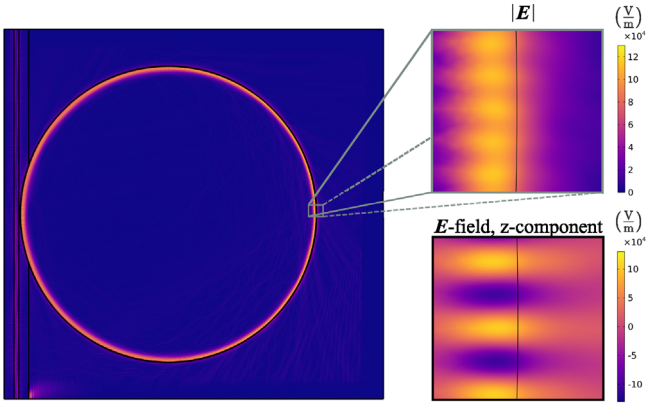

Fig. 5. Electric-field intensity of the uncoated microresonator coupled to the optical fiber at the resonance wavelength 786.92 nm, and zoomed mode profiles, including the z-component of the electric field around the microresonator surface.

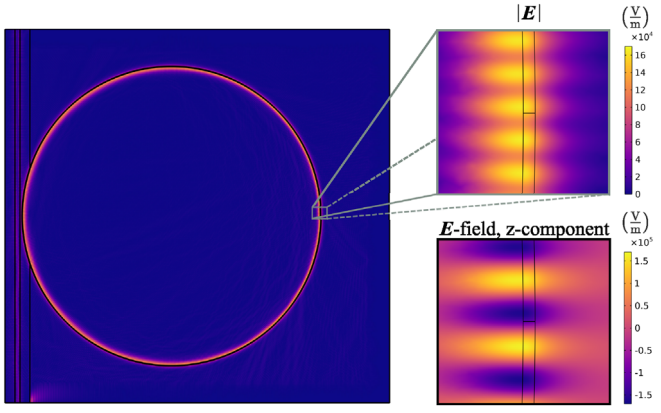

Figure 6. The electric-field at the resonance wavelength $\lambda_{res,PS} = 789.38$ nm for the PS-coated microresonator coupled to the optical fiber, with zoomed mode profile of the E_z field near the microresonator surface.

5.2 $CsPbI_3$ coating

Finally, the $CsPbI_3$-coated microresonator is modeled and numerically analyzed. Here, the first and most important step is to identify the desired excitonic–photonic coupling between the microresonator WGM and the perovskite nanocoating. Based on the eigenmode simulations in Ref. [41], a wavelength range from 886 nm to 900 nm with a step size of 0.01 nm is explored. It is observed that at $\lambda_{res,CsPbI_3} = 886.60$ nm an effective excitonic–photonic coupling between the microresonator photonic mode and the $CsPbI_3$ coating excitonic mode is achieved. In this configuration, the hybrid excitonic–photonic mode is mainly confined within the nanocoating rather than in the silica core. However, since the refractive index of the $CsPbI_3$

Table 1. Figures of merit for the sensing performance of the uncoated, 100 nm PS-coated, and $CsPbI_3$-coated microresonators.

	d_x (nm)	λ_{res} (nm)	Mode no.	T (%)	Q_f	V_{mode} (μm^2)	$\lvert \boldsymbol{E} \rvert$ (V/m)
Uncoated	350	786.92	335	85.56	1.81×10^4	73.88	0.87×10^5
PS-coated	400	789.38	339	92.39	2.09×10^4	54.79	1.52×10^5
$CsPbI_3$-coated	350	886.60	321	51.89	6.21×10^4	40.29	3.20×10^5

coating is not much higher than that of water, the evanescent tail of the electric field still penetrates strongly into the surrounding medium, and the field intensity at the sensing location is significantly increased (cf. Fig. 7).

It is worth mentioning that the electric field distribution $|\boldsymbol{E}|$ for the $CsPbI_3$-coated microresonator looks different compared to the usual WGM electric field distributions, observed in both uncoated and PS-coated microresonators. The reason behind this is the presence of the hybrid excitonic-photonic mode in the $CsPbI_3$-coated microresonator, which, due to the excitonic mode, does not depict the characteristic teardrop shapes typically present in WGM electric field distributions. Such teardrop features are visible in the E_z component resulting from the WGM of the microresonator; however, in this case, the E_x and E_y electric field components associated with the excitonic mode of the $CsPbI_3$ coating modify the electric field distribution $|\boldsymbol{E}|$.

In the next step, the coupling distance for the $CsPbI_3$-coated microresonator is optimized, and an optimal value of $d_{x,CsPbI_3} = 350$ nm is found, yielding a transmitted power of 51.9% within the microresonator. Although this transmitted power is substantially lower than in the uncoated and PS-coated cases, the other sensing-related figures of merit are markedly improved. As a result, the $CsPbI_3$-coated microresonator, due to the hybrid excitonic–photonic coupling, still outperforms the other configurations in terms of sensing functionality. All key sensing figures of merit for the three investigated configurations (uncoated, PS-coated, and $CsPbI_3$-coated microresonators) are calculated and presented in Table 1. As can be seen, the Q_f is about 2.4 times larger in the case of the $CsPbI_3$-coated microresonator compared to the uncoated case, which is a direct consequence of the hybrid excitonic–photonic mode formation. In addition, the relatively high refractive index of the $CsPbI_3$ coating reduces the mode volume by about 45% compared to the uncoated microresonator.

A critical figure of merit for quantifying the performance of our optical biosensor is the electric-field strength at the sensing location $|\boldsymbol{E}|$, as this parameter determines the excess polarizability of the exosome and, consequently, the magnitude of the resonance wavelength shift. Figure 8 shows the electric-field intensity distribution at the respective resonance wavelengths for all three configurations (uncoated, PS-coated, and $CsPbI_3$-coated microresonators) along the radial direction, zoomed into a region close to the microresonator surface. It is evident that the addition of the nanocoating shifts the optical mode profile towards the surface, thereby enhancing the field intensity at the sensing location. Moreover, the results show that the perovskite nanocoating both confines the mode and amplifies the electric-field intensity at the sensing location by a factor of 2.11 compared to the PS-coated case and by a factor of 3.68 compared to the uncoated case. This pronounced improvement is directly related to the formation of the hybrid excitonic–photonic mode within our proposed biosensor.

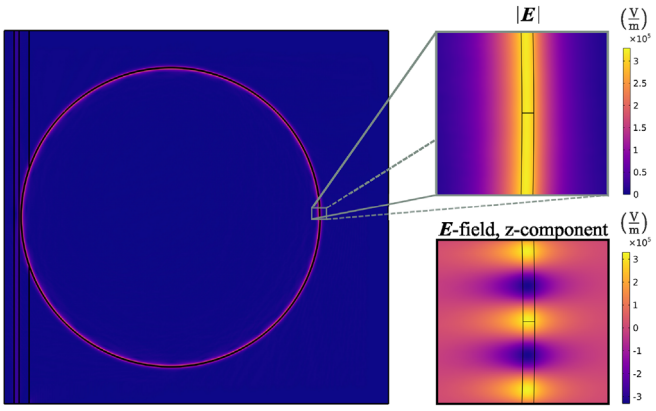

Fig. 7. Electric-field intensity of the $CsPbI_3$-coated microresonator coupled to the optical fiber at the resonance wavelength 886.60 nm. Zoomed views show $|\boldsymbol{E}|$ and E_z near the resonator surface.

The results summarized in Table 1 further underline the effectiveness of the $CsPbI_3$ coating compared to both the uncoated and the PS-coated microresonator.

Since the $CsPbI_3$ coating is lossy, there is a natural concern that absorption in the coating layer could degrade the microresonator performance. To address this, we evaluate the absorption within the nanocoating by integrating the total power dissipation density over the coated region. Because the model is two-dimensional, the integration is carried out over a cross-section, and the resulting absorbed power in the coating region is reported per unit length (W/m). It is found that the absorption losses in the coating are generally low, on the order of 10^{-5} W/m. However, as shown in Figure 9, the local absorption losses within the water medium are significantly larger in the presence of the coating, which is a direct consequence of the larger evanescent field tails (i.e. penetration depth) into the water solution.

6 Exosome detection and characterization

The final and decisive figure of merit for evaluating the $CsPbI_3$-coated microresonator is the resonance-wavelength shift induced by a single exosome. To this end, healthy

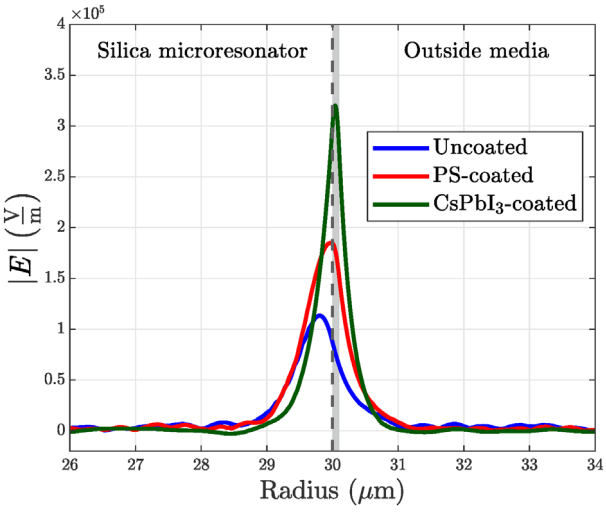

Fig. 8. Electric-field intensity along the resonator radius at the resonance wavelengths for the uncoated, PS-coated, and $CsPbI_3$-coated microresonators. The gray area represents the coating region for both PS- and $CsPbI_3$-coated cases.

(H), borderline (B), and cancerous (C) exosomes are placed in the immediate vicinity of the uncoated, PS-coated, and $CsPbI_3$-coated microresonators, and the corresponding resonance-wavelength shifts are computed for all three sensor configurations. The resulting shifts are summarized in Table 2. It can already be seen that the $CsPbI_3$ coating increases the exosome-induced wavelength shift by more than a factor of two compared to the uncoated microresonator.

Figure 10 shows the electric-field intensity distribution for the three microresonators when a single healthy exosome is placed at the sensing position. The field enhancement in the vicinity of the exosome is visibly stronger for the coated cases, with the $CsPbI_3$-coated microresonator exhibiting the largest local field intensity. Note that for the $CsPbI_3$-coated case the color scale (vertical) is adjusted, as the peak field is almost twice as large as in the uncoated and PS-coated configurations. The polarization magnitude $|\boldsymbol{P}|$ inside the healthy exosome is also shown in Figure 10 using the horizontal colorbars. The $CsPbI_3$-coated microresonator yields a significantly larger polarization response inside the exosome, presenting values approximately 3 and 6 times higher than for the PS-coated and uncoated cases, respectively (see the different color scales ranges).

When the exosome health state is changed (healthy, borderline, and cancerous), the induced polarization within the exosome varies. This behavior was observed for all three microresonator configurations. Figure 11 shows the polarization response inside healthy, borderline and cancerous exosomes placed at the sensing location for the $CsPbI_3$-coated microresonator. A monotonic increase in the polarization magnitude is observed, starting from the healthy case to the borderline case, reaching the largest values for the cancerous case. This trend is consistent with larger resonance wavelength shifts calculated for the borderline and cancerous cases, as shown in Table 2 for all the three microresonators.

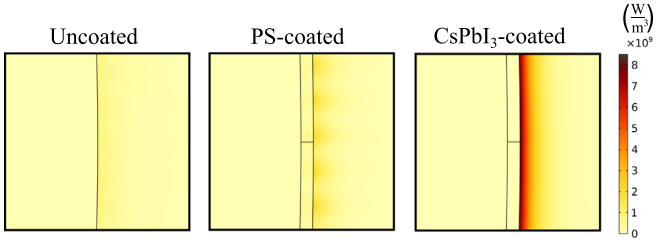

Fig. 9. Power dissipation density profiles for the uncoated, 100 nm PS-coated, and $CsPbI_3$-coated microresonators on the equator of the microresonator surface.

Table 2. Resulting resonance-wavelength shifts for a single exosome placed at the immediate vicinity of each microresonator, for healthy (H), borderline (B), and cancerous (C) exosomes.

	$\Delta\lambda_H$ (pm)	$\Delta\lambda_B$ (pm)	$\Delta\lambda_C$ (pm)
Uncoated	0.75	0.87	1.08
PS-coated	1.08	1.33	1.58
$CsPbI_3$-coated	1.79	2.02	2.38

Results from Table 2 show that compared to the uncoated microresonator, the PS-coated sensor exhibits increases of 44.0%, 52.9%, and 46.3% in the resonance-wavelength shift for the healthy, borderline, and cancerous exosomes, respectively. Changing the coating material to $CsPbI_3$ leads to even larger enhancements: the corresponding shifts increase by 138.7%, 132.2%, and 120.4% for the healthy, borderline, and cancerous exosomes, respectively, relative to the uncoated case. Thus, both coatings improve the absolute sensitivity, with the perovskite nanocoating providing the largest enhancement.

Our main goal, however, is not only to detect the presence of a single exosome but also to discriminate its health state. In this context, the separation between the wavelength shifts associated with different health classes is crucial. For the uncoated microresonator, the difference between the cancerous and healthy cases is $\Delta\lambda_C - \Delta\lambda_H = 0.33$ pm. This separation increases to 0.50 pm for the PS-coated microresonator and to 0.59 pm for the $CsPbI_3$-coated microresonator, i.e. an additional increase of about 18% in the H–C contrast compared to the PS case. Similar trends are observed for the H–B and B–C separations.

These results demonstrate that the presence of the nanocoating not only increases the absolute resonance-wavelength shifts but also enhances the contrast between healthy, borderline, and cancerous exosomes. In particular, the $CsPbI_3$-coated microresonator offers both the largest overall shifts and the largest separation between health states. This validates that our proposed excitonic–photonic hybrid microresonator is capable of identifying the health state of a single exosome and therefore supports liquid-biopsy based, non-invasive, early-stage cancer diagnostics.

In the present work, a single exosome is positioned at the equatorial region of the resonator to maximize

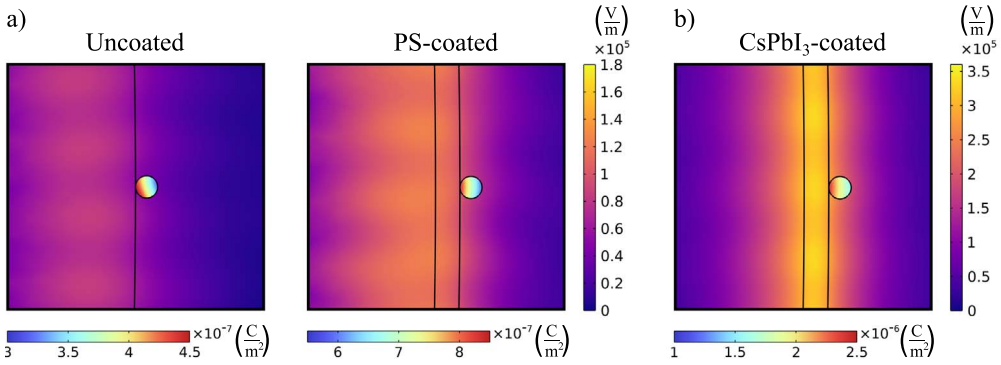

Fig. 10. Electric-field intensity distribution when a single healthy exosome (H) is placed at the immediate vicinity of (a) the uncoated and the PS-coated microresonators and (b) the $CsPbI_3$-coated microresonator, plotted together with the polarization magnitude $|\boldsymbol{P}|$ inside the exosome. The vertical colorbars denote $|\boldsymbol{E}|$. Note that the color scale for the $CsPbI_3$-coated microresonator is different and the maximum value is twice as high as in the other cases. The horizontal colorbars indicate $|\boldsymbol{P}|$ inside the healthy exosome. Note the different magnitude ranges for each plot.

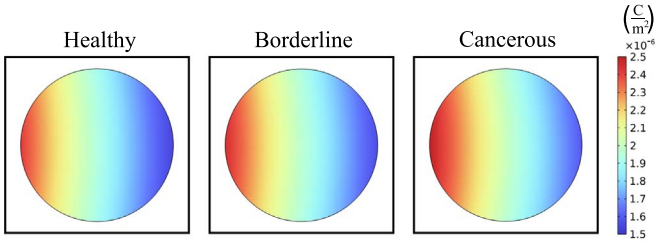

Fig. 11. Polarization in the healthy, borderline and cancerous exosomes next to the $CsPbI_3$-coated microresonator.

sensitivity, assuming ideal binding and precise placement at the sensing interface. To assess the impact of non-ideal placement, a complementary study on the same biosensor platform was conducted, in which the exosome position was systematically varied in both radial and angular directions (see [54]), assuming a 50 nm exosome with $n_{\text{eff}} = 1.3847$ [36]. The results show that, while radial displacement leads to a pronounced reduction in the sensing response for all configurations due to the rapid evanescent-field decay, the $CsPbI_3$-coated microresonator exhibits a markedly reduced dependence on small angular position variations compared to the uncoated and PS-coated cases, with an almost unchanged local electric field (variation $\approx 0.3\%$), as well as nearly invariant resonance wavelength shift and induced exosome polarization [54], as can be seen in Figure 12. This behavior is attributed to the more uniform near-surface field distribution associated with the hybrid photonic–excitonic mode supported by the perovskite coating.

From a practical perspective, the reduced angular dependence of the proposed $CsPbI_3$-coated microresonator, specifically designed for single-exosome detection, relaxes the requirement for precise exosome positioning at a single optimal location and supports more robust sensing under realistic conditions. At the same time, the results confirm that maintaining the exosome in close proximity to the resonator surface remains essential for maximizing sensitivity, highlighting the importance of surface-functionalization strategies for effective exosome trapping [54]. Scenarios involving multiple simultaneously adsorbed exosomes are beyond the scope of this study, as the sensing concept is based on controlled delivery and positioning of individual exosomes, for example through microfluidic-assisted transport and ligand-based surface functionalization.

7 Conclusion

In this work, we have proposed and numerically demonstrated an excitonic–photonic hybrid whispering-gallery-mode microresonator as an ultra-sensitive optical biosensor for single-exosome detection and health-state classification. A 30 μm silica microdisk with a 100 nm nanocoating was modeled in an aqueous environment and excited via a single-mode fiber using full-wave driven-mode computational electromagnetics simulations in Comsol Multiphysics. To the best of our knowledge, this represents the first full-field driven-mode study of coated WGM microresonators with explicit fiber coupling for biosensing applications. In parallel, we developed a physics-based framework to determine the effective refractive index of individual exosomes as a function of their protein and nucleic-acid content, combining the Barer relation for the lumen, a core–shell exosome geometry, and volume-averaged D/E retrieval from full-wave simulations. This yields dispersive effective refractive indices $n_{\text{eff}}^{(\text{H,B,C})}(\lambda)$ for healthy, borderline, and cancerous exosomes and provides, to the best of our knowledge, the first ERI-based description of exosomes explicitly parameterized by health state.

On the photonic side, we systematically compared uncoated, PS-coated, and $CsPbI_3$-coated microresonators. The PS nanocoating was shown to enhance the sensing performance by increasing the quality factor Q_{f} by $\sim$15%, reducing the mode volume V_{mode} by 25.8%, and amplifying the electric field at the sensing location by a factor of 1.75 relative to the uncoated case. Building on our previous eigenmode screening [36, 41], we then identified a configuration in which a $CsPbI_3$ perovskite nanocoating exhibits strong excitonic–photonic coupling with the silica WGM

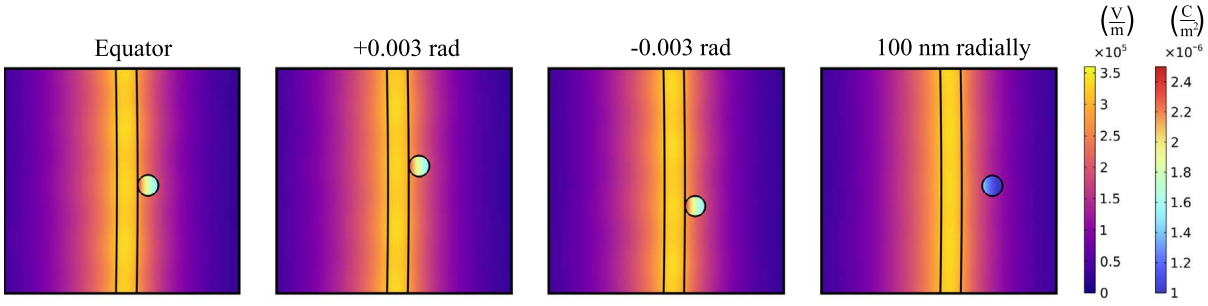

Fig. 12. Electric-field intensity distribution and the polarization magnitude $|\boldsymbol{P}|$ inside a single exosome for the $CsPbI_3$-coated microresonator, when the exosome position is varied in both angular (± 0.003 rad) and radial (100 nm shifted) directions.

at $\lambda_{res,CsPbI_3} \approx 886.6$ nm. The resulting hybrid mode is largely confined within the perovskite nanocoating while maintaining a strong evanescent tail in water. Despite the intrinsic material loss of the perovskite, this configuration yields the highest Q_f (a factor ∼2.4 above the uncoated case), the smallest V_{mode} (reduced by ∼45%), and the strongest surface field enhancement (electric-field intensity increased by factors of 2.11 and 3.68 relative to the PS-coated and uncoated resonators, respectively), while also establishing a more spatially uniform near-surface field distribution at the sensing interface. To the best of our knowledge, this is the first report of an engineered excitonic–photonic mode coupling in a perovskite-coated WGM microresonator specifically tailored for biosensing.

Coupling the exosome ERI model to the hybrid microresonators, we quantified the resonance-wavelength shifts induced by single healthy, borderline, and cancerous exosomes placed at the sensing position. Both PS and $CsPbI_3$ nanocoatings substantially increase the absolute resonance shifts compared to the uncoated resonator, with the perovskite-coated device providing the largest enhancement. For example, the healthy-exosome shift increases from 0.75 pm (uncoated) to 1.08 pm (PS-coated) and 1.79 pm ($CsPbI_3$-coated), corresponding to enhancements of 44% and 139%. At the same time, the separation between health states is improved: the difference between cancerous and healthy exosomes, $\Delta\lambda_C - \Delta\lambda_H$, increases from 0.33 pm (uncoated) to 0.50 pm (PS-coated) and 0.59 pm ($CsPbI_3$-coated). These results show that the proposed architecture does not merely detect the presence of an exosome but also amplifies the contrast between healthy, borderline, and cancerous ERI values. Taken together, this constitutes, to the best of our knowledge, the first demonstration of an optical WGM biosensor that exploits excitonic–photonic hybridization to both detect and characterize the health state of single exosomes. Importantly, the hybrid-mode-induced field redistribution also reduces the dependence of the sensing response on angular exosome positioning, thereby enhancing robustness against non-ideal binding conditions [54].

The presented study establishes a complete, simulation-based design workflow that links biochemical composition (protein/NA content) to exosome ERI and ultimately to measurable resonance signatures in a realistic, fiber-coupled WGM biosensor. Future work will focus on translating these designs into fabricated devices, including the controlled deposition and stabilization of $CsPbI_3$ nanocoatings on silica microdisks, and on the experimental validation of the predicted single-exosome shifts in microfluidic environments. In this context, controlled delivery and isolation of individual exosomes, e.g., via microfluidic-assisted transport combined with ligand-based surface functionalization, will be essential to ensure precise positioning at the sensing interface and to mitigate multi-particle effects, which are beyond the scope of the present study. Beyond cancer diagnostics, the proposed framework can be extended to other EV subtypes and disease markers, and combined with statistical or machine-learning classifiers to enable robust ERI-based phenotyping of heterogeneous exosome populations. More broadly, our results highlight the potential of excitonic materials as functional nanocoatings for next-generation photonic biosensors operating at the single-particle level.

Funding

Funded by the Deutsche Forschungsgemeinschaft (DFG, German Research Foundation) – Project number 4102100053004. We acknowledge support by the Open Access Publication Fund of the University of Duisburg-Essen.

Conflicts of interest

The authors declare no conflicts of interest associated to this work.

Data availability statement

Data underlying the results presented in this paper are not publicly available at this time but may be obtained from the authors upon reasonable request.

Author contribution statement

Modeling: M.M.G., B.B., M.J.; Simulation: M.M.G., M.J.; Investigation: M.M.G., M.J.; Conceptualization: M.J.; Funding acquisition: M.J., D.E.; Supervision: D.E., M.J.; Writing and editing: M.M.G., M.J., D.E.; Review: D.E., M.J.

References

1 Vollmer F, Braun D, Libchaber A, Khoshsima M, Teraoka I, Arnold S, Protein detection by optical shift of a resonant microcavity, *Appl. Phys. Lett.* **80**, 4057–4059 (2002). https://doi.org/10.1063/1.1482797.
2 Arnold S, Khoshsima M, Teraoka I, Holler S, Vollmer F, Shift of whispering-gallery modes in microspheres by protein

adsorption, *Opt. Lett.* **28**, 272–274 (2003). https://doi.org/10.1364/OL.28.000272.
3 Jiang X, Qavi AJ, Huang SH, Yang L, Whispering-gallery sensors, *Matter.* **3**, 371–392 (2020). https://doi.org/10.1016/j.matt.2020.07.008.
4 Loyez M, Adolphson M, Liao J, Yang L, From whispering gallery mode resonators to biochemical sensors, *ACS Sens.* **8**, 2440–2470 (2023). https://doi.org/10.1021/acssensors.2c02876.
5 Lopez-Yglesias X, Gamba JM, Flagan RC, The physics of extreme sensitivity in whispering gallery mode optical biosensors, *J. Appl. Phys.* **111**, 084701 (2012). https://doi.org/10.1063/1.3698319.
6 Foreman MR, Swaim JD, Vollmer F, Whispering gallery mode sensors, *Adv. Opt. Photonics.* **7**, 168–240 (2015). https://doi.org/10.1364/AOP.7.000168.
7 Su J, Label-free biological and chemical sensing using whispering gallery mode optical resonators: past, present, and future, *Sensors.* **17**, 540 (2017). https://doi.org/10.3390/s17030540.
8 Vitullo DLP, Zaki S, Jones DE, Sumetsky M, Brodsky M, Coupling between waveguides and microresonators: the local approach, *Opt. Express.* **28**, 25908–25914 (2020). https://doi.org/10.1364/OE.399978.
9 Wu X, Zhu C, Wang Y, Fan X, Micro/nano lasers for biomolecular sensing and cellular analysis, *Photonic Sens.* **15**, 250123 (2025). https://doi.org/10.1007/s13320-024-0711-7.
10 Toropov N, Cabello G, Serrano MP, Gutha RR, Rafti M, Vollmer F, Review of biosensing with whispering-gallery mode lasers, *Light Sci. Appl.* **10**, 42 (2021). https://doi.org/10.1038/s41377-021-00471-3.
11 Anwar AR, Mur M, Humar M, Microcavity- and microlaser-based optical barcoding: A review of encoding techniques and applications, *ACS Photon.* **10**, 1202–1224 (2023). https://doi.org/10.1021/acsphotonics.2c01611.
12 Baaske MD, Foreman MR, Vollmer F, Single-molecule nucleic acid interactions monitored on a label-free microcavity biosensor platform, *Nature Nanotech.* **9**, 933–939 (2014). https://doi.org/10.1038/nnano.2014.180.
13 Su J, Label-free single exosome detection using frequency-locked microtoroid optical resonators, *ACS Photon.* **2**, 1241–1245 (2015). https://doi.org/10.1021/acsphotonics.5b00142.
14 Giannetti A, Berneschi S, Baldini F, Cosi F, Conti GN, Soria S, Performance of eudragit coated whispering gallery mode resonator-based immunosensors, *Sensors* **12**, 14604–14611 (2012). https://doi.org/10.3390/s121114604.
15 Daaboul GG et al., Digital detection of exosomes by interferometric imaging, *Sci. Rep.* **6**, 37246 (2016). https://doi.org/10.1038/srep37246.
16 Dragovic RA et al., Sizing and phenotyping of cellular vesicles using nanoparticle tracking analysis, *Nanomedicine.* **7**, 780–788 (2011). https://doi.org/10.1016/j.nano.2011.04.003.
17 Imanbekova M, Suarasan S, Lu Y, Jurchuk S, Wachsmann-Hogiu S, Recent advances in optical label-free characterization of extracellular vesicles, *Nanophotonics.* **11**, 2827–2863 (2022). https://doi.org/10.1515/nanoph-2022-0057.
18 Kalluri R, LeBleu VS, The biology, function, and biomedical applications of exosomes, *Science* **367**, eaau6977 (2020). https://doi.org/10.1126/science.aau6977.
19 Chen Y, Luh F, Ho Y, Yen Y, Exosomes: a review of biologic function, diagnostic and targeted therapy applications, and clinical trials, *J. Biomed. Sci.* **31**, 67 (2024). https://doi.org/10.1186/s12929-024-01055-0.
20 Yu D et al., Exosomes as a new frontier of cancer liquid biopsy, *Mol. Cancer.* **21**, 56 (2022). https://doi.org/10.1186/s12943-022-01509-9.
21 Irmer B, Chandrabalan S, Maas L, Bleckmann A, Menck K, Extracellular vesicles in liquid biopsies as biomarkers for solid tumors, *Cancers* **15**, 1307 (2023). https://doi.org/10.3390/cancers15041307.
22 Tai Y, Chen K, Hsieh J, Shen T, Exosomes in cancer development and clinical applications, *Cancer Sci.* **109**, 2364–2374 (2018). https://doi.org/10.1111/cas.13697.
23 Hoshino A et al., Extracellular vesicle and particle biomarkers define multiple human cancers, *Cell* **182**, 1044–1061.e18 (2020). https://doi.org/10.1016/j.cell.2020.07.009.
24 Shen H et al., Exosomal proteins: new targets for early diagnosis and treatment of cancer, *Front. Immunol.* **16**, 1613494 (2025). https://doi.org/10.3389/fimmu.2025.1613494.
25 Rupert DLM et al., Effective refractive index and lipid content of extracellular vesicles revealed using optical waveguide scattering and fluorescence microscopy, *Langmuir.* **34**, 8522–8531 (2018). https://doi.org/10.1021/acs.langmuir.7b04214.
26 de Rond L et al., Refractive index to evaluate staining specificity of extracellular vesicles by flow cytometry, *J. Extracell. Vesicles.* **8**, 1643671 (2019). https://doi.org/10.1080/20013078.2019.1643671.
27 Welsh JA et al., Towards defining reference materials for measuring extracellular vesicle refractive index, epitope abundance, size and concentration, *J. Extracell. Vesicles.* **9**, 1816641 (2020). https://doi.org/10.1080/20013078.2020.1816641.
28 Shao L et al., Detection of single nanoparticles and lentiviruses using microcavity resonance broadening, *Adv. Mater.* **25**, 5616–5620 (2013). https://doi.org/10.1002/adma201302572.
29 Capocefalo A, Quintiero E, Conti C, Ghofraniha N, Viola I, Droplet lasers for smart photonic labels, *ACS Appl. Mater Interfaces.* **13**, 51485–51494 (2021). https://doi.org/10.1021/acsami.1c14972.
30 Thomson CA, Popczyk A, Schubert M, Gather MC, Biointegrated microlasers: technologies, applications, and emerging developments, *Optica* **12**, 1311–1326 (2025). https://doi.org/10.1364/OPTICA.563263.
31 Guo P et al., Room–temperature red–green–blue whispering–gallery mode lasing and white–light emission from cesium lead halide perovskite ($CsPbX_3$, X = Cl, Br, I) microstructures, *Adv. Optical Mater.* **6**, 1700993 (2018). https://doi.org/10.1002/adom.201700993.
32 Li Q et al. Lasing from reduced dimensional perovskite microplatelets: Fabry-pérot or whispering-gallery-mode?, *J. Chem. Phys.* **151**, 211101 (2019). https://doi.org/10.1063/1.5127946.
33 Zhang L, Li X, Song Y, Zou B, Ultrafast antisolvent growth of single-crystal $CsPbBr_3$ microcavity for whispering-gallery-mode lasing, *Nanomaterials* **13**, 2116 (2023). https://doi.org/10.3390/nano13142116.
34 Lanty G, Bréhier A, Parashkov R, Lauret JS, Deleporte E, Strong exciton–photon coupling at room temperature in microcavities containing two-dimensional layered perovskite compounds, *New J. Phys.* **10**, 065007 (2008). https://doi.org/10.1088/1367-2630/10/6/065007.
35 Polimeno L et al., Room temperature polariton condensation from whispering gallery modes in $CsPbBr_3$ microplatelets, *Adv. Mater.* **36**, e2312131 (2024). https://doi.org/10.1002/adma.202312131.

36 Jalali M, Erni D, Early stage, label-free detection of breast cancer based on exosome's protein content alteration, in *Proceedings SPIE 12139, Optical Sensing and Detection VII*, 2022, **121390G**. https://doi.org/10.1117/12.2621062.

37 Bessif B, Jalali M, Erni D, Investigating the efficient light coupling into a microdisk in presence and absence of a polymer coating, in Proceedings SPIE 13006, *Biomedical Spectroscopy, Microscopy, and Imaging III*, 2024, 130060Y. https://doi.org/10.1117/12.3022110.

38 Garcia MM, Bessif B, Jalali M, Erni D, Detection and characterization of exosomes via a polystyrene-coated silica microresonator, *EPJ Web Conf.* **335**, 04002 (2025). https://doi.org/10.1051/epjconf/202533504002.

39 Polyanskiy MN, Refractiveindex.info database of optical constants, *Sci. Data.* **11, 94** (2024). https://doi.org/10.1038/s41597-023-02898-2.

40 Ilican S, Zor M, Caglar Y, Caglar M, Optical characterization of the CdZn $(S_{1-x}\ Se_x)_2$ thin films deposited by spray pyrolysis method, *Optica Applicata.* **36**, 29–37 (2006).

41 Jalali M, Erni D, Enhancing the sensitivity of silica microresonator-based biosensors through adding a perovskite coating, in *International Conference on Single-Molecule, Sensors and Nano Systems (S^3IC)*, 2023, 61.

42 van der Pol E et al., Absolute sizing and label-free identification of extracellular vesicles by flow cytometry, *Nanomedicine.* **14**, 801–810 (2018). https://doi.org/10.1016/j.nano.2017.12.012.

43 Nagle JF, Tristram-Nagle S, Structure of lipid bilayers, *Bioch. Biophys. Acta.* **1469**, 159–195 (2000). https://doi.org/10.1016/S0304-4157(00)00016-2.

44 González CM, Pizarro-Guerra G, Droguett F, Sarabia M, Artificial biomembrane based on DPPC – investigation into phase transition and thermal behavior through ellipsometric techniques, *Bioch. Biophys. Acta.* **1848**, 2295–2307 (2015). https://doi.org/10.1016/j.bbamem.2015.07.001.

45 Parkkila P, Elderdfi M, Bunker A, Viitala T, Biophysical characterization of supported lipid bilayers using parallel dual-wavelength surface plasmon resonance and quartz crystal microbalance measurements, *Langmuir.* **34**, 8081–8091 (2018). https://doi.org/10.1021/acs.langmuir.8b01259.

46 Kienle DF, de Souza JV, Watkins EB, Kuhl TL, Thickness and refractive index of DPPC and DPPE monolayers by multiple-beam interferometry, *Anal. Bioanal. Chem.* **406**, 4725–4733 (2014). https://doi.org/10.1007/s00216-014-7866-9.

47 Mapar M, Sjöberg M, Zhdanov VP, Agnarsson B, Höök F, Label-free quantification of protein binding to lipid vesicles using transparent waveguide evanescent-field scattering microscopy with liquid control, *Biomed. Opt. Express.* **14**, 4003–4016 (2023). https://doi.org/10.1364/BOE.490051.

48 Daimon M, Masumura A, Measurement of the refractive index of distilled water from the near-infrared region to the ultraviolet region, *Appl. Opt.* **46**, 3811–3820 (2007). https://doi.org/10.1364/AO.46.003811.

49 Barer R, Refractometry and interferometry of living cells, *J. Opt. Soc. Am.* **47**, 545–556 (1957). https://doi.org/10.1364/JOSA.47.000545.

50 Zhao H, Brown PH, Schuck P, On the distribution of protein refractive index increments, *Biophys. J.* **100**, 2309–2317 (2011). https://doi.org/10.1016/j.bpj.2011.03.004.

51 Jia X et al., Enabling online determination of the size-dependent RNA content of lipid nanoparticle-based RNA formulations, *J. Chromatogr. B.* **1186**, 123015 (2021). https://doi.org/10.1016/j.jchromb.2021.123015.

52 Tatischeff I, Extracellular vesicle-DNA: the next liquid biopsy biomarker for early cancer diagnosis? *Cancers.* **15**, 1456 (2023). https://doi.org/10.3390/cancers15051456.

53 Pleet ML, et al. Extracellular vesicle refractive index derivation utilizing orthogonal characterization, *Nano Lett.* **23**, 9195–9202 (2023). https://doi.org/10.1021/acs.nanolett.3c00562.

54 Garcia MM, Bessif B, Jalali M, Erni D, Effect of sensing location on the sensing functionality of coated microresonators for exosome detection, submitted to *Proceedings SPIE 14086: Optical Sensing and Detection IX*, (2026).